Lensa: Jurnal Kependidikan Fisika
Penerbit: Universitas Pendidikan Mandalika
https://e-journal.undikma.ac.id/index.php/Lensa/index

June 2024. Vol.12, No.1
e-ISSN:2686-0937
pp.60-77

Co-Precipitation Synthesis and Analysis of Co and Zn Doped Barium M-Hexaferrites

Dwi Pangga[1], Haerul Pathoni[2,*], Suprianto[3]

[1] Physics Education Department, Universitas Pendidikan Mandalika, Mataram, Indonesia
[2] Physics Education Department, Universitas Jambi, Kota Jambi, Indonesia
[3] Physics Education Department, Universitas Islam Madura, Pamekasan, Indonesia

Corresponding Author: haerul_pathoni@unja.ac.id

Abstract

Barium hexaferrite ($BaFe_{12}O_{19}$) is a material of significant interest due to its wide range of applications. In this study, we synthesized barium M-hexaferrites ($BaFe_{12-2x}Co_xZn_xO_{19}$) powders through the co-precipitation method, starting from $BaCO_3$ and $FeCl_3.6H_2O$ powders, with Co and Zn powders used as dopant materials. The variations in x values were set at 0, 0.2, 0.4, 0.6, 0.8, and 1. Our findings indicate that the co-precipitation method is highly effective for synthesizing barium M-hexaferrites ($BaFe_{12-2x}Co_xZn_xO_{19}$) nanomaterials, which contain more than 89% iron elements and have an average particle size of 50 nm. The Differential Thermal Analysis (DTA) and Thermogravimetric Analysis (TGA) reveal that phase transformations occur at temperatures of 285°C and in the range of 750-840°C. Further analysis using the Rietveld refinement method demonstrates that the barium M-hexaferrite phase begins to form at relatively low temperatures, with the most optimal yield observed at x = 0.4. At temperatures exceeding 740°C, there is a tendency to form a single-phase α-Fe_2O_3 (hematite). The introduction of Co and Zn as dopant ions results in only minor changes to the lattice parameters of the basic hexagonal crystal structure. This comprehensive study underscores the viability of the co-precipitation method for producing high-quality barium M-hexaferrites and provides valuable insights into the effects of Co and Zn doping on the structural and thermal properties of these materials.

Keywords: Barium hexaferrites; Co-precipitation method; Nanomaterials; Doping effects; Phase transformation.

How to cite: Pangga, D., Pathoni, H., & Suprianto, S. (2024). Co-Precipitation Synthesis and Analysis of Co and Zn Doped Barium M-Hexaferrites. *Lensa: Jurnal Kependidikan Fisika, 12*(1), 60-77. doi:https://doi.org/10.33394/j-lkf.v12i1.11732

INTRODUCTION

The development of advanced magnetic materials has been a focal point of materials science research due to their critical applications in electronic devices, magnetic storage systems, and other technological advancements. Barium M-Hexaferrite ($BaFe_{12}O_{19}$) is a widely studied magnetic material because of its magnetic stability. However, its magnetic properties can be further enhanced by doping with transition metals, making it a suitable candidate for high-density magnetic recording and other high-performance magnetic applications.

Hexaferrites are a fascinating class of magnetic materials characterized by their hexagonal crystal structure, formed by closely packed layers of oxygen ions. Within these structures, trivalent metal cations occupy interstitial spaces, and larger ions, such as Ba^{2+}, substitute into the oxygen layers, significantly influencing the material's properties (Hähsler et al., 2020). Hexaferrites are categorized into various types—M, W, Y, X, U, and Z—based on their distinct chemical and crystal structures (Pullar, 2012). Among these, barium hexaferrites ($BaFe_{12}O_{19}$) are notable for their exceptional magnetic properties and have been the subject of extensive research and industrial application (Awadallah et al., 2016).

Barium hexaferrites are recognized for their high magnetic saturation, significant coercivity, elevated Curie temperature, excellent corrosion resistance, and remarkable chemical stability (Lin et al., 2018; Shao et al., 2018). These properties are further enhanced by a large magneto-crystalline anisotropy constant (Primc et al., 2009) and high cohesive strength (Kanagesan et al., 2011). The combination of these magnetic properties, along with the relatively straightforward and cost-effective synthesis processes, makes barium hexaferrites highly attractive for a range of applications, particularly in electromagnetic absorption technologies (Zhao et al., 2017).

The unique physical and chemical properties of barium hexaferrite ($BaFe_{12}O_{19}$) have garnered significant study interest due to their applicability in various devices and technologies. For instance, they are used as components in electronic devices (Koutzarova et al., 2013), magnetic recording media with high density (Wang et al., 2017), microwave devices (Gultom et al., 2020), and as critical components in speakers, electric motors, and generators (Rusianto et al., 2015). Additionally, they serve as catalysts in chemical reactions (Abbasi et al., 2016) and have applications in the audio-video recording industry (Almessiere et al., 2019). One promising application is in the development of high-density magnetic recording solutions for big data storage, utilizing barium hexaferrites in recording tapes (Kaur et al., 2016). More recently, their potential use in military defense systems, particularly as absorbers of electromagnetic waves in aircraft radar systems, has been explored (Anand et al., 2020). Future advancements in magnetic microwave devices, which are expected to be smaller, lighter, and more efficient, heavily rely on the development of advanced ferrite materials (Harris et al., 2009).

Previous studies have highlighted the potential of barium M-hexaferrite $BaFe_{12}O_{19}$ as an effective anti-radar material, comparable to Fe_3O_4 with Ni/Zn amplifiers (Wu et al., 2008). This material demonstrates significant microwave absorption capabilities (Feng et al., 2007). However, a high coercivity field remains a challenge, as it necessitates a high external field to achieve zero magnetization, which is undesirable for certain applications. The high coercivity also enhances anisotropic properties, weakening absorption capabilities. One approach to address this issue is substituting the ions in the M-phase with other metal cations of similar size, such as Zn^{2+}, Ti^{4+}, Co^{2+}, Ga^{3+}, and Al^{3+} (Rösler et al., 2003). Specifically, doping with Co/Zn ions is expected to reduce the magnetic anisotropy of barium M-hexaferrite $BaFe_{12-2x}Co_xZn_xO_{19}$ by disrupting the magnetic moment direction, leading to a more random domain structure. Moreover, reducing the powder (grain) size to the nano-scale can lower the high coercivity field. Effective inter-grain interactions at grain sizes smaller than 380 nm significantly impact the three fundamental magnetic properties: remanent magnetization, coercivity fields, and maximum energy products (Cheng et al., 2003).

In this study, we synthesized nano-sized barium M-hexaferrite by substituting Fe ions in the M-phase with Co/Zn dopant ions. Barium hexaferrites exhibit various types—M, W, U, X, Y, and Z—each influenced by the stoichiometric variables of the constituent elements and the sintering temperature during the synthesis process (Ahmed et al., 2008). Therefore, a comprehensive identification of the structural aspects is crucial to ensure the formation of the desired material. It is anticipated that the substitution of Co/Zn dopant ions for Fe ions will not alter the basic structure

of the $BaFe_{12}O_{19}$ base material, given the similar dimensions of the substituting and substituted materials.

In this research, the materials were synthesized using the coprecipitation method with variations in the concentration of Co/Zn dopant ions in barium M-hexaferrite ($BaFe_{12}O_{19}$). The synthesized materials were examined through various analytical techniques: thermal analysis (TA) to assess decomposition and formation phases, X-Ray Fluorescence (XRF) to determine elemental composition, X-Ray Diffraction (XRD) to identify crystal phases, Transmission Electron Microscopy (TEM) to visualize microstructure, and Fourier Transform Infrared Spectroscopy (FTIR) to understand the substitution process of dopant ions in the crystal structure. The study primarily investigates the effects of Co/Zn ion substitution on the microstructure, phase, and crystal structure of barium M-hexaferrite, with the variable x set at 0, 0.2, 0.4, 0.6, 0.8, and 1. The sintering temperatures were 200°C, 270°C, 840°C, and 900°C, each with a holding time of 4 hours.

Aim of the Study

The primary aim of this study is to investigate the effects of Co/Zn ion substitution on the microstructure phase and crystal structure of barium M-hexaferrite (BaFe12O19). The study focuses on understanding how varying the concentration of Co/Zn dopant ions (with x values set at 0, 0.2, 0.4, 0.6, 0.8, and 1) impacts the formation, thermal stability, and structural properties of the resulting hexaferrite. By analyzing the synthesis process using the co-precipitation method and subsequent sintering at different temperatures, the research aims to optimize the conditions for producing high-quality barium M-hexaferrites with desirable magnetic and structural characteristics.

METHODS

For the synthesis of barium M-hexaferrite ($BaFe_{12-2x}Co_xZn_xO_{19}$), the following materials were employed: barium carbonate ($BaCO_3$) powder and Iron (III) chloride hexahydrate ($FeCl_3.6H_2O$) served as the primary base materials. Cobalt (Co) powder and zinc (Zn) proanalyst (PA) powder were used as the doping materials, with variations of x = 0; 0.2; 0.4; 0.6; 0.8; and 1.0. These variations in x correspond to the molecular formula of the barium-based salts, allowing for a systematic study of the doping effects on the resulting hexaferrite. The purity and quality of the chemicals were ensured by using proanalyst grade reagents.

The synthesis of $BaFe_{12-2x}Co_xZn_xO_{19}$ was performed using the coprecipitation method, which is known for producing high-purity and homogeneous materials (see Figure 1).

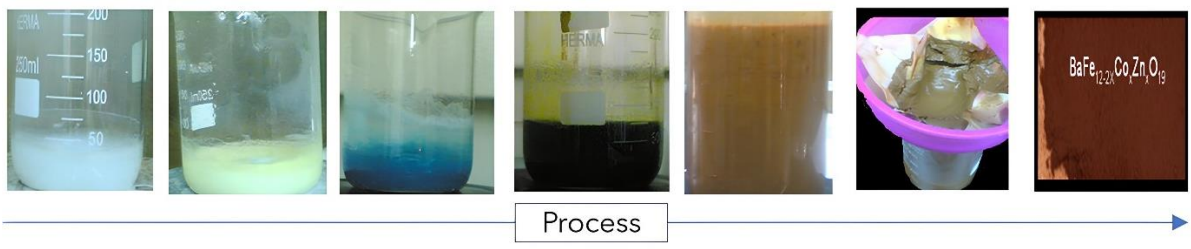

Figure 1. Synthesis process of $BaFe_{12-2x}Co_xZn_xO_{19}$ powder via coprecipitation

Initially, $BaCO_3$, Co, and Zn powders were dissolved in hydrochloric acid (HCl) with a molarity of 12.063 M (PA 99.9%). Separately, $FeCl_3.6H_2O$ powder was dissolved in distilled water to create a clear solution. Both solutions were thoroughly mixed using a magnetic stirrer to ensure homogeneity. The key step in this process was the addition of ammonium hydroxide (NH_4OH, 6.5 M, PA 99.9%), which facilitated the coprecipitation of the desired compounds. The precipitation process was meticulously monitored to achieve high homogeneity in the precipitate. The resulting precipitate was allowed to settle before being washed with distilled water to neutralize the pH to 7. The washed material was then filtered and dried at 80°C for two hours, yielding the precursor material for further analysis.

The phase formation of the synthesized $BaFe_{12-2x}Co_xZn_xO_{19}$ was characterized using X-ray diffraction (XRD) analysis. A Multi-Purpose Diffractometer (MPD), such as the JEOL-3530 or Philips X'Pert MPD, was utilized for this purpose. This step was crucial for confirming the successful synthesis of the barium M-hexaferrite precursor. The XRD patterns obtained were compared against standard reference patterns to identify the phases present in the material. To further understand the thermal stability and phase transition behavior, thermal analysis was conducted using Differential Thermal Analysis (DTA) and Thermogravimetric Analysis (TGA). These analyses helped determine the optimal sintering temperatures, which were found to range between 25°C and 1200°C, depending on the specific value of x in the doping variable.

Post-sintering, the elemental composition of the samples was analyzed using X-ray fluorescence (XRF) spectroscopy. This technique provided quantitative data on the elemental makeup of the doped barium hexaferrite. Following XRF analysis, the phase composition of the sintered samples was re-evaluated using XRD. The XRD data were processed with Rietveld refinement methods using Rietica software, allowing for precise determination of phase quantities. Additionally, MAUD (Materials Analysis Using Diffraction) software was employed to analyze changes in lattice parameters due to the substitution of Co and Zn ions. These analyses were critical for understanding the structural modifications induced by doping.

Scanning Electron Microscopy (SEM) and Transmission Electron Microscopy (TEM) were utilized to examine the microstructure and grain size of the synthesized $BaFe_{12-2x}Co_xZn_xO_{19}$. SEM provided detailed images of the surface morphology, while TEM offered insights into the internal structure at the nanoscale. These techniques were essential for confirming the uniformity and size distribution of the grains, which are crucial factors affecting the magnetic properties of hexaferrites. Fourier-transform infrared (FTIR) spectroscopy was also performed to identify the chemical bonds and molecular structures present in the samples. FTIR analysis helped confirm the successful incorporation of Co and Zn dopants into the hexaferrite lattice by detecting specific vibrational modes corresponding to these elements.

The comprehensive set of analyses—TA, XRD, XRF, SEM, TEM, and FTIR—provided a detailed understanding of the effects of Co and Zn doping on the structural and compositional properties of barium M-hexaferrite. By correlating the results from different characterization techniques, the optimal doping level (x) for achieving the desired phase and properties of $BaFe_{12-2x}Co_xZn_xO_{19}$ was determined.

These findings are pivotal for tailoring the magnetic properties of hexaferrites for specific applications in electronic and magnetic devices.

RESULTS AND DISCUSSION

Synthesis of Barium M-Hexaferrite

The outcomes of the DTA/TGA analysis are depicted in Figure 2. The initial tests were conducted at concentrations of x = 0 and x = 0.6. DTA/TGA provides insights into the energy and mass changes associated with temperature variations. The thermal behavior, whether exothermic or endothermic, along with mass changes, indicates phase transformations. Specifically, exothermic events are indicative of crystallization processes, while endothermic events point to decomposition or melting processes.

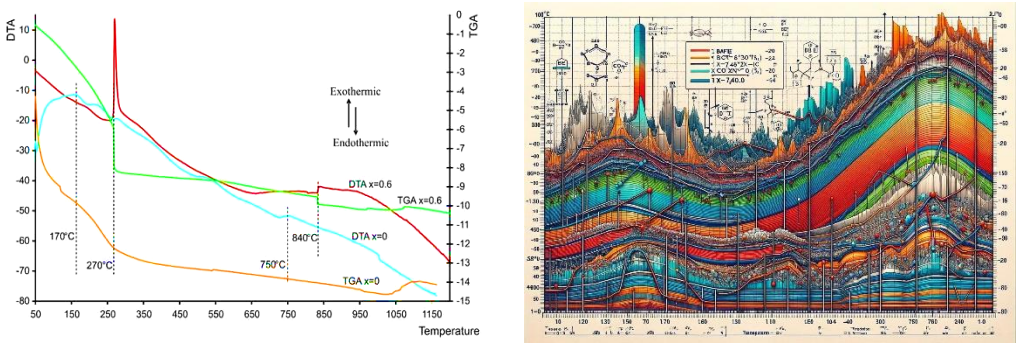

Figure 2. The results of the DTA/TGA of $BaFe_{12-2x}Co_xZn_xO_{19}$ (x = 0 and x = 0.6).

Figure 2 illustrates the DTA/TGA results for $BaFe_{12-2x}Co_xZn_xO_{19}$ (x = 0 and x = 0.6). Before incorporating Co/Zn ions, the barium M-hexaferrite phase was $BaFe_{12}O_{19}$ (x = 0). After substitution (x = 0.6), the phase transitioned to $BaFe_{10.8}Co_{0.6}Zn_{0.6}O_{19}$. Both phases maintain the same structure, but the latter shows increased stability based on the transformation temperature. Figure 2 also reveals a shift in the phase transformation temperature between x = 0 and x = 0.6. Both substituted and unsubstituted barium M-hexaferrite exhibit exothermic behavior and mass reduction. The initial mass reduction and exothermic event (T ≤ 285°C) are likely due to the evaporation of water and gas, forming the $BaFe_{12-2x}Co_xZn_xO_{19}$ phase. The second exothermic process (T = 740 - 850°C), accompanied by mass reduction, is attributed to the release of oxalate bonds, resulting in the formation of a more stable phase. There is also a tendency for mass to increase in the range T = 1050 - 1100°C for both x values, indicating a reaction with air to form a new phase.

Significant changes in the properties of the barium M-hexaferrite material are due to the presence of Co/Zn dopant ions at the Fe site. The addition of Co/Zn dopant shifts the phase transformation temperatures from 170 to 270°C and from 750 to 840°C for x = 0 and x = 0.6, respectively. This demonstrates that the substitution of Co/Zn dopant ions at the Fe site has taken place, enhancing the stability of the phase transformation temperature.

At a concentration of x = 0.6, an exothermic event followed by a sharp mass reduction provides several insights. The initial exothermic event and sharp mass reduction occur at T = 270 - 285°C, after which the mass stabilizes up to T = 840°C. Similarly, the second exothermic event and mass reduction occur at T = 840°C, followed by a stable mass. This indicates a crystallization process, where bond

dissociation and mass loss occur until a stable phase is achieved, leading to a stable formation energy and no further mass reduction.

Elemental Identification

In the synthesis of barium M-hexaferrite powder using the coprecipitation method, the final product comprises $BaFe_{10}CoZnO_{19}$ (solid) along with 36 NH_4Cl (aqueous), 88 H_2O (liquid), CO_2 (gas), and 3 H_2 (gas) when x = 1. During the calcination or sintering process, all liquids evaporate, leaving only the $BaFe_{10}CoZnO_{19}$ phase as a solid. These resulting phases are polymorphic. To achieve phase homogeneity, a sintering process is required. Based on thermal analysis results for samples with x = 0 and x = 0.6, sintering was performed at various values of x at temperatures of 200°C, 270°C, 700°C, 840°C, 900°C, 1000°C, and 1200°C for four hours.

The sintering process resulted in noticeable changes in the concentration of the variable x, which subsequently affected the color of the synthesized powders. As depicted in Figure 3, the color of the powders darkened progressively with an increasing concentration of Co/Zn dopant ions at sintering temperatures of T ≤ 270°C. This color change signifies a higher content of cobalt powder, which is characterized by a darker black hue. For instance, the powder with no dopant ions (x = 0) retained a lighter color, while the powder with the highest concentration of dopant ions (x = 1) exhibited the darkest color.

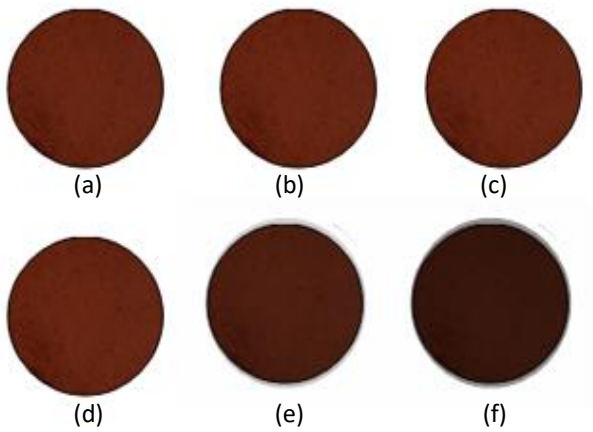

Figure 3. The influence of varying concentration x on the color change of $BaFe_{12-2x}Co_xZn_xO_{19}$ precursor powder at a sintering temperature of T ≤ 270°C is observed as follows: (a) x = 0; (b) x = 0.2; (c) x = 0.4; (d) x = 0.6; (e) x = 0.8; and (f) x = 1.

Specifically, the variations in the dopant concentration are illustrated in the different shades of the powders in Figure 3, shows the precursor powders at various levels of x: (a) x = 0, (b) x = 0.2, (c) x = 0.4, (d) x = 0.6, (e) x = 0.8, and (f) x = 1. The color transitions from a lighter brown at lower concentrations of Co/Zn dopants to a deep black at higher concentrations. This gradient in color intensity highlights the increasing presence of Co/Zn ions, which plays a crucial role in the structural and compositional attributes of the synthesized barium M-hexaferrite powders.

At a sintering temperature of T ≥ 840°C, the material exhibits a blackish-brown coloration. This observation suggests that all H_2O and HCl components are entirely eliminated, as evidenced by the XRF results (Table 1).

Table 1. X-Ray Fluorescence (XRF) analysis of the elemental precursor $BaFe_{10,8}Co_{0,6}Zn_{0,6}O_{19}$ for x = 0.6

Element	T = 80°C, 2 h, Composition (at%)	T = 270°C, 4 h, Composition (at%)	T = 840°C, 4 h, Composition (at%)
Cl	9.36	1.30	0
Fe	89.11	97.03	87.19
Co	0.54	0.69	2.73
Zn	0.50	0.53	2.29
Ba	0.45	0.45	7.79

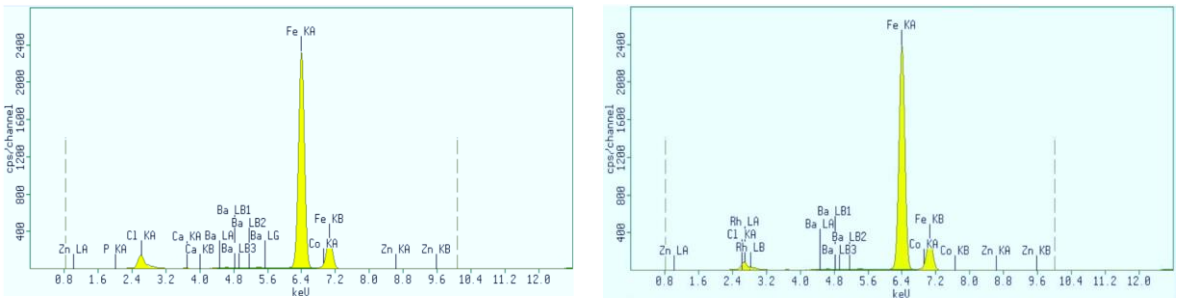

(a) (b)

Figure 4. The XRF spectra of $BaFe_{10.8}Co_{0.6}Zn_{0.6}O_{19}$ powder were obtained after drying the samples under the following conditions: (a) at 80°C for 2 hours, and (b) at 270°C for 4 hours.

The XRF analysis depicted in Figure 4 confirms the presence of elements essential to the formation of the barium M-hexaferrite phase, specifically Ba, Fe, Co, and Zn, at treatment temperatures of T = 80°C and T = 270°C. In their oxide forms, Co and Zn are likely to form Co_3O_4 and ZnO, respectively, while Fe forms Fe_2O_3 (hematite). The oxidation states of these ions are inferred to be +3 (Fe^+), Co^{3+}/Co^{2+}, and Zn^{2+} based on the similarity in their ionic radii: Fe^{3+} has a radius of 0.065 nm, Co^{3+}/Co^{2+} has radii of 0.055/0.075 nm, and Zn^{2+} has a radius of 0.074 nm (Pathak et al., 2014). The substitution of these ions can result in changes to particle dimensions, observable through XRD analysis and microstructural examination. The sintering process, driven by a substitutional ionic diffusion mechanism, facilitates the transformation of hematite, barium oxide, and other oxides ($BaO.6Fe_2O_3$) into barium M-hexaferrite $BaFe_{12-2x}Co_xZn_xO_{19}$.

Identification of Phases

In this research, barium M-hexaferrite was doped with Co^{3+}/Co^{2+} and Zn^{2+} ions. Due to the similar ionic radii and the relatively low dopant concentrations ($0 \leq x \leq 1$), the fundamental structure of barium M-hexaferrite is expected to remain unchanged. The primary anticipated effect is a slight shift in the diffraction pattern peak positions (angle 2θ) because of lattice parameter variations, as described by Bragg's equation ($2d_{hkl}\sin\theta_B = n\lambda$).

Refinement results using $BaFe_{12}O_{19}$ and α-Fe_2O_3 as inputs on the dried precursors showed that the $BaFe_{12}O_{19}$ phase composition ranged from 31% to 55%. These results were promising due to a relatively low goodness-of-fit (GoF) value, although the large displacement sample values and the full-width at half-maximum (FWHM) peak shapes, which remained super Lorentzian, posed challenges. The low

GoF value resulted from the measured data's low intensity, peaking at only 130, complicating the Rietveld method solution.

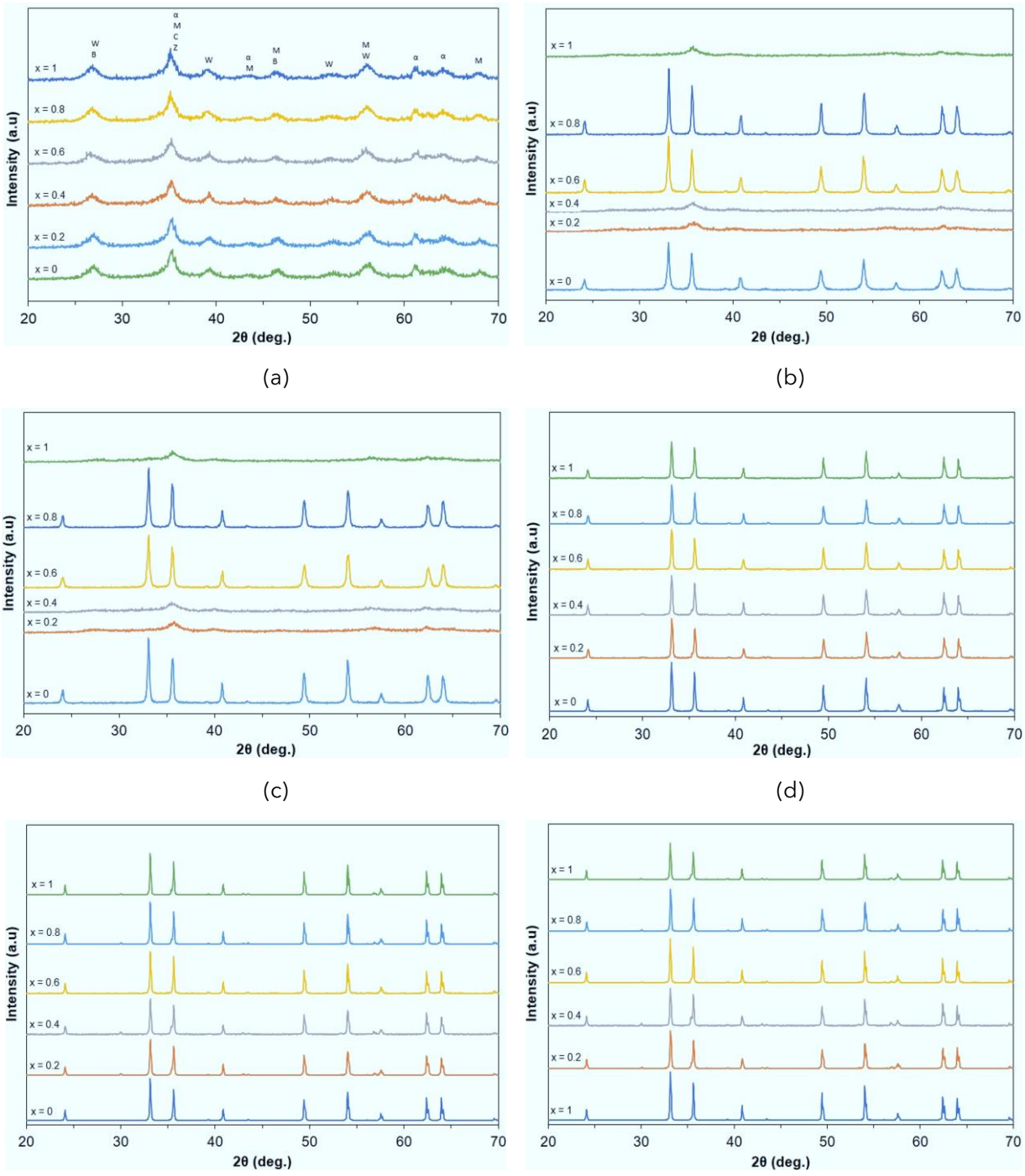

Figure 5. The XRD pattern of precursor $BaFe_{12-2x}Co_xZn_xO_{19}$ with composition of substitution x: (a) after 2 h drying, T = 80°C (B = BaO, Z = ZnO, C = Co_3O_4, M = M-type, α = α-Fe_2O_3 phase, W = W-type); (b) 4 h sintering, T = 200°C (α = α-Fe_2O_3 phase); (c) 4 h sintering, T = 270°C (α = α-Fe_2O_3 phase); (d) 4 h sintering, T = 270°C (Z = ZnO, C = Co_3O_4, M = M-type, α = α-Fe_2O_3 phase, W = W-type); (e) 4 h sintering, T = 840°C; and (f) 4 h sintering, T = 900°C.

To elucidate the formed phases, standard data were utilized, as illustrated in Figure 5a. The diffraction pattern appeared similar across different x values, exhibiting widened peaks that suggest small particle sizes and a rough, more amorphous peak shape. Search matching with six standard datasets indicated that the dry precursor comprises multiple phases. These phases, formed during coprecipitation, have not yet transformed into more stable phases. The variety of dry precursor phases is affected by the polymorphic characteristics of barium hexaferrite, which encompasses M, Y, W, X, Z, and U types. According to DTA/TGA data, phase transformation happens at a sintering temperature below 285°C, with an exothermic peak observed at 270°C.

During the high-temperature sintering processes at 200°C and 270°C, significant differences are observed in the diffraction patterns for various substitution levels of x. These differences are likely caused by the incomplete substitution of Fe sites with Co/Zn dopant ions, leading to an unstable crystal structure. This instability is evident in the XRD spectrum, as shown in Figures 5b and 5c, where the diffraction patterns at 200°C are very similar to those at 270°C. These observations are consistent with the DTA/TGA results, which show that the first phase transition occurs below 285°C, with exothermic peaks at 170°C for x = 0 and 270°C for x = 0.6. The diffraction patterns for x = 0, 0.6, and 0.8 differ from those for x = 0.2, 0.4, and 1, indicating that the phase remains unstable due to the effects of ion doping and sintering.

According to the 2-input refinement results, samples with x = 0, 0.6, and 0.8 tend to form a hematite (α-Fe_2O_3) phase, while samples with x = 0.2, 0.4, and 1 show the formation of an M-hexaferrite phase up to 83.19%. This trend is consistent for sintering precursors at 200°C and 270°C (x = 0.2, 0.4, 1) with a maximum intensity of 110. Although the GoF value obtained is low (<4%), the phase formation is in line with the refinement results, taking into account the low intensity, significant sample displacement values, and peak shapes in FWHM. The search match method, shown in Figure 5d, reveals the presence of barium W-hexaferrite, Co_3O_4, and ZnO, alongside barium M-hexaferrite and hematite phases, indicating phase instability.

As shown in Figures 5e and 5f, a more stable diffraction pattern develops following further phase transformation decomposition within the temperature range of 740-850°C. The diffraction pattern observed at 840°C sintering is distinct from those seen at 200°C, 270°C, or during the drying process. Nonetheless, the diffraction patterns at higher sintering temperatures (900°C and 840°C) are almost identical, with only slight differences in intensity. These results indicate that at temperatures ≤285°C, two unstable phases are formed, while a stable single-phase (hematite) is present at temperatures ≥750°C.

The XRD patterns for all x variables at 840°C and 900°C show minimal variation. No peak position shifts occur due to the presence of Co/Zn dopant ions. In this state, the dopant ion substitution likely involves Co^{3+} and Zn^{2+} ions (not Co^{2+}), with ionic radii of Co^{3+} = 0.055 nm, Co^{2+} = 0.075 nm, and Zn^{2+} = 0.074 nm. Thus, the substitution of Co^{3+} and Zn^{2+} ions for Fe^{3+} ions (radius = 0.065 nm) should not alter lattice parameters, as the substituting ion dimensions (0.0645 nm) closely match those of the Fe^{3+} ion. Based on Bragg's equation $2d_{hkl}\sin\theta_B = n\lambda$, d_{hkl} remains unchanged, keeping the 2θ position fixed, resulting in no peak position shifts in the diffraction pattern (Figures 5e and 5f).

The refinement analysis reveals that during the exothermic event and initial mass reduction (T ≤ 285°C), both barium M-hexaferrite and hematite phases are formed. In the second mass reduction and exothermic event (750-840°C), a phase transition takes place, resulting in a single-phase hematite. At T ≤ 285°C, the formation of the barium M-hexaferrite phase is inconsistent across all x variables. The substitution at x = 0.4 shows the most favorable results, with the barium M-hexaferrite phase forming at 80°C, 200°C, and 270°C, achieving percentages of 49.58%, 81.52%, and 83.19%, respectively. The second mass reduction (750-840°C) allows for decarbonation and CO_2 release (Suasmoro et al., 2000) due to slow oxidation during decomposition (Rösler et al., 2003). The first mass reduction, coupled with an exothermic process, results from gas loss and energy absorption to break bonds in $BaFe_{12}O_{19}$ ($BaO.6Fe_2O_3$) into BaO and 6Fe2O3. Experimental results confirm the formation of single-phase α-Fe_2O_3 at 700°C, 840°C, 900°C, and 1000°C, while the BaO phase remains undetected by XRD due to its minimal fraction compared to α-Fe_2O_3.

Refinement and search match results indicate that Co/Zn dopant ion substitution at x = 0.4 yields the best outcomes. Sintering significantly contributes to barium M-hexaferrite formation. At the drying temperature (Figure 5a), phase identification using the search match method reveals the presence of various substituted M-hexaferrite phases, including BaO, ZnO, Co_3O_4, M-type ($BaFe_{12}O_{19}$), α-Fe_2O_3, and W-type ($BaCo_2Fe_{16}O_{27}$). Multiple phases likely result from co-precipitation, with the presence of six basic barium hexaferrite crystal structures (M, W, Y, X, Z, and U) leading to more complex phases (Ahmed et al., 2008).

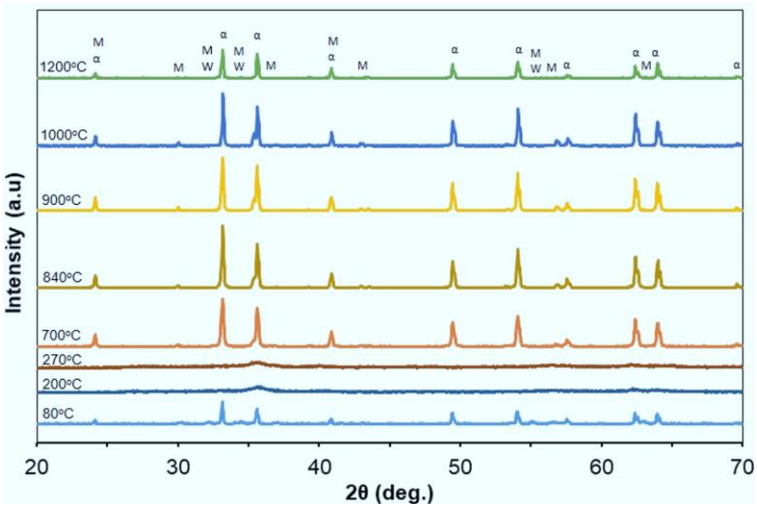

Figure 6. XRD pattern of precursor $BaFe_{11,2}Co_{0,4}Zn_{0,4}O_{19}$ sintered at various temperatures

Figure 6 shows the XRD patterns for $BaFe_{11.2}Co_{0.4}Zn_{0.4}O_{19}$ at various temperatures. The data suggests that higher temperatures cause phase transformation and reduce oxygen content. This is indicated by the change of the W-type hexaferrite phase (27 oxygen atoms per unit cell) into hematite at 700°C, 840°C, 900°C, and 1000°C. At 1200°C, the material becomes a mix of M-type hexaferrite (19 oxygen atoms per unit cell) and W-type, with a higher amount of the M-type phase. Furthermore, Figure 6 highlights unique behaviors for the Co/Zn dopant substitution at x = 0.4 compared to other levels. The barium M-hexaferrite

phase is shown by a low-intensity diffraction pattern, while a high-intensity pattern indicates the hematite phase. Barium M-hexaferrite appears at 80°C, 200°C, and 270°C. Even at 1200°C, up to 70% of the barium M-hexaferrite phase is present, unlike other substitution levels. This implies that x = 0.4 is the most effective level for forming the barium M-hexaferrite phase.

Microstructure Analysis of Barium M-Hexaferrit

Figure 7's TEM results reveal microstructural changes due to different sintering temperatures. Higher sintering temperatures cause the precursor M-hexaferrite particles to grow larger. This growth is due to the formation of liquid bridges between particles, consistent with XRD results that show narrower and sharper peaks as sintering temperatures rise. The TEM image of the precursor $BaFe_{12-2x}Co_xZn_xO_{19}$ shows a particle size distribution akin to the crystal size seen in XRD results, with sizes in the nanometer range. These particles' nanomaterial nature allows their physical and chemical properties to change with size, offering numerous opportunities to manipulate or create new properties not present in bulk materials.

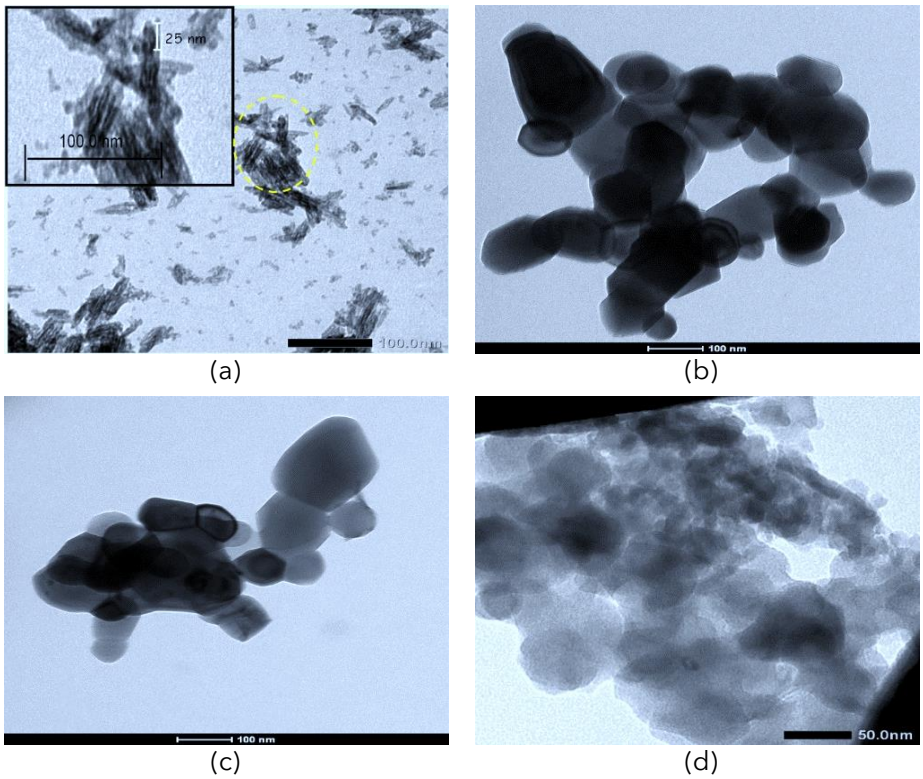

(a) (b) (c) (d)

Figure 7. The TEM results of precursor $BaFe_{12-2x}Co_xZn_xO_{19}$: (a) x = 0,4 T = 270°C; (b) x = 0,6 T = 840°C; (c) x = 0,6 T = 900°C; and (d) x = 0,4 T = 1200°C.

TEM analysis reveals that the particle structure reflects the fundamental crystal structure of BaFe12O19, typically hexagonal with axes a = b ≠ c, α = ß = 90, and γ = 120. Significant microstructural differences are observed at x = 0.4 and x = 0.6: at x = 0.4, the shape appears more elongated, whereas at x = 0.6, it is more circular. This observation corresponds with the XRD analysis results depicted in Figures 7 (b) and (c) for hematite phases, and Figures 7 (a) and (d) for hematite and barium M-hexaferrite phases. The variation in phases causes the microstructure in Figures 7

(a) and (d) to be more elongated since the c-axis of the barium M-hexaferrite lattice parameter (23.183 Å) is much longer than the a and b axes (a = b = 5.892 Å).

In Figure 7(a), particles appear less clustered compared to Figures 7 (b), (c), and (d), due to the low sintering temperature of this precursor (T = 270°C), preventing the formation of liquid bridges. The enlarged TEM image in Figure 7(a) of a 70 nm particle in the longitudinal direction shows smaller particles reaching 25 nm in the longitudinal direction. In contrast, Figures 7(b), (c), and (d) display particles clustering together due to liquid bridge formation at higher sintering temperatures. In Figures 7(b) and (c), the particle shapes are round, as hematite forms at these temperatures, where the axes a, b, and c are relatively similar in size compared to the M-hexaferrite barium lattice parameters. Figure 7(d) shows elongated and nearly spherical particles due to the predominant formation of M-hexaferrite at 1200°C, with some remaining hematite phase. Overall, the average particle size is around 50 nm, implying that one particle consists of about 22 units of barium M-hexaferrite cells (c-axis = 23.183 Å) for elongated shapes, and about 36 units of hematite cells (c = 13.747 Å) for spherical shapes.

Given the ionic radii of Co^{3+}/Co^{2+} (0.055/0.075 nm) and Zn^{2+} (0.074 nm) compared to Fe^{3+} (0.065 nm), replacing Fe3+ ions with Co/Zn dopant ions is expected to alter the dimensions of the lattice parameters. It is established that within a single unit cell, 12 Fe ions are replaced by Co/Zn dopant ions. This substitution likely increases the lattice parameter size, which subsequently enlarges the particle size due to the aggregation of multiple crystal cell units within a single particle.

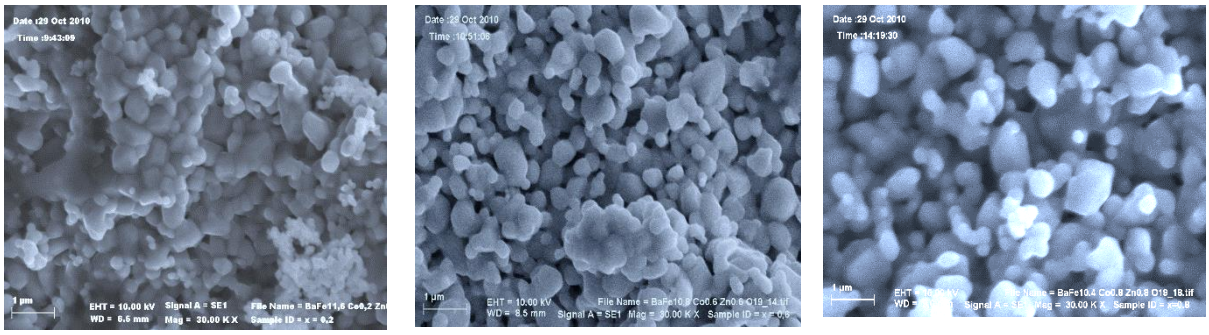

(a) (b) (c)

Figure 8. SEM analysis of precursor $BaFe_{12-2x}Co_xZn_xO_{19}$ (T = 1000°C) for the substitution composition: (a) x = 0.2; (b) x = 0.6; dan (c) x = 0.8.

SEM observations shown in Figure 8 confirm that Co/Zn doping enhances lattice parameters. These images reveal that, at a magnification of 30k×, the powder size progressively increases with higher Co/Zn dopant concentrations, ranging from x = 0.2 to x = 0.6 and x = 0.8. However, accurately determining the powder sizes from SEM images is difficult because the powders cluster into nanoscale sizes, as shown by TEM images. Both TEM and SEM analyses verify that the crystal structure remains hexagonal and that nanomaterials have been effectively synthesized. The observed changes are limited to the lattice parameters, with grain size expanding in correlation with the increasing Co/Zn dopant levels. This outcome suggests the potential for producing soft magnetic materials with low coercivity (Hc). Ferrite-based materials with low Hc are promising for applications in high and ultra-high

frequency soft magnetic materials (Zhang et al., 2020), and they are also suitable for use as anti-radar materials with high absorption values (Bayrakdar et al., 2013).

Analysis of the Co/Zn Dopant Ion Substitution Mechanism

FTIR analysis was performed to investigate the process of Co/Zn ion substitution (Figure 9).

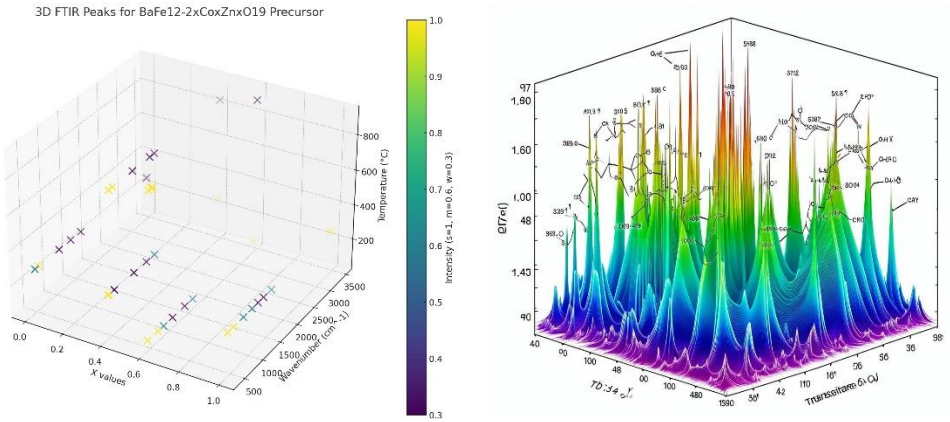

Figure 9. FTIR absorption pattern (in 3D) of precursor $BaFe_{12-2x}Co_xZn_xO_{19}$

The precursor of $BaFe_{12-2x}Co_xZn_xO_{19}$ shows the presence of various bonds, including those other than metal bonds. For the variable x, the peaks observed at 421, 436, and 575 cm^{-1} for x = 0.4 (T = 270°C), and peaks at 478 and 575 cm^{-1} for x = 0.4 (T = 840°C), are associated with metal bonds (Fe-O) in the barium M-hexaferrite and hematite phases. These peaks correspond to characteristic vibrations below 800 cm^{-1}, indicative of oxygen-metal bonds in the mixture. Moreover, peaks within the 800 to 1650 cm^{-1} range represent the characteristic vibration absorption of the carbonate group (CO_3^{2-}). The vibrational features at 450 and 570 cm^{-1} signify the Fe-O vibration bond, a characteristic of barium ferrite (Ting & Wu, 2010).

The results of the FTIR analysis of Co/Zn dopant concentration and flashing temperature are summarized in Table 2.

Table 2. The FTIR transmission peaks ($1/\lambda=cm^{-1}$) for the precursor $BaFe_{12-2x}Co_xZn_xO_{19}$

T = 80°C, 2h	T = 270°C, 4h			T = 840°C, 4h	T = 900°C, 4h
x = 0.6	x = 0	x = 0.4	x = 1	x = 0.4	x = 0.6
421 (s)	482 (m)	421 (s)	421 (s)	478 (s)	478 (s)
687 (s)	574 (s)	436 (s)	575 (s)	575 (s)	552 (s)
841 (m)	1084 (w)	575 (w)	849 (m)	1076 (w)	575 (s)
1080 (w)	1385 (w)	1080 (w)	1088 (m)	1520 (w)	3422 (w)
1408 (w)	1647 (w)	1408 (w)	1254 (w)	1640 (w)	-
1628 (m)	3422 (w)	1628 (m)	1408 (w)	3449 (w)	-
3383 (s)	3448 (w)	3422 (s)	1628 (m)	-	-
-	-	-	3387 (s)	-	-
-	-	-	3421 (s)	-	-

Note: absorption intensity (s=strong, m=medium, w=weak)

The result in Table 2 indicate that higher sintering temperatures lead to fewer peaks. Specifically, for the same Co/Zn dopant ion concentration, the number of peaks decreases as the sintering temperature increases for both x = 0.4 and x = 0.6.

This observation aligns with the XRD analysis, which shows that temperatures above 740°C tend to produce a single phase of hematite. The formation of this single phase is due to the disruption of interparticle interactions at higher sintering temperatures. Conversely, at a constant temperature of 270°C, the number of peaks in the 1000 to 1800 cm^{-1} range is relatively consistent. The spectra within the 1000 to 1600 cm^{-1} range correspond to $BaCO_3$ bonds, while those between 1000 and 1800 cm^{-1} correspond to BaO and Fe_2O_3 bonds, which are components of barium M-hexaferrite. As the value of x increases (from 0 to 1) at the same temperature, peak intensity decreases, indicating that Co/Zn dopant ions are replacing Fe ions.

The vibration absorption characteristics can be divided into three wave number groups: V < 800 cm^{-1}, V = 800-1650 cm^{-1}, and V = 3350-3450 cm^{-1}. Within the V < 800 cm^{-1} range, multiple peaks consistently appear at both low and high temperatures. Barium M-hexaferrite shows vibrational features at V = 546 and 582 cm^{-1} in this range (Yu & Liu, 2006). Research has shown that Co_3O_4-ZnO exhibits vibrational characteristics at V = 673 cm^{-1}, with Co-O bonds at V = 579 and 674 cm^{-1} (Ai & Jiang, 2009), indicating the presence of Co/Zn bonds.

Figure 9 and Table 2 illustrate that Co-O and Zn-O bonds are found in all test samples, with characteristics at V = 687 cm^{-1} and V = 552-575 cm^{-1}. However, it is difficult to distinguish dopant ionic bonds at T ≥ 270°C because V = 421-575 cm^{-1} also represents the Fe-O bond. An interesting peak at V = 687 cm-1 is observed only in the sample with x = 0.6 (T = 80°C), indicating the presence of Co_3O_4 and ZnO bonds. In the dry precursor, there are still some Fe-O bonds indicating the barium phase M-hexaferrite and hematite due to the oxide phase from coprecipitation.

At high sintering temperatures (T ≥ 740°C), peaks in the V = 800-1650 cm^{-1} range disappear, indicating the formation of a single phase. This decrease in peaks at high temperatures aligns with the XRD results (Figure 6), which show only the hematite phase formation. The hematite phase (Fe-O bond) is identifiable in the FTIR spectrum at wavelengths < 800 cm^{-1} across all sintering temperatures. Additionally, the FTIR spectrum in the V = 3350-3450 cm^{-1} range corresponds to chemical bonds undetectable by XRD, likely small amounts of -OH and FeO-OH bonds, which eventually disappear at high sintering temperatures.

CONCLUSION

The coprecipitation method for synthesizing barium M-hexaferrite $BaFe_{12-2x}Co_xZn_xO_{19}$ has demonstrated notable efficacy, yielding the highest results of 83.19% at x = 0.4 and a temperature of 270°C, and 70.55% at a temperature of 1200°C. Detailed analysis using Differential Thermal Analysis/Thermogravimetric Analysis (DTA/TGA) and X-Ray Diffraction (XRD) has revealed that the sintering process at temperatures equal to or greater than 740°C tends to promote the formation of a hematite (α-Fe2O3) phase. The average particle size obtained from this synthesis approach is around 50 nm. Introducing cobalt (Co) and zinc (Zn) dopant ions at the iron (Fe) sites does not alter the basic hexagonal crystal structure of barium M-hexaferrite. However, as the concentration of these dopant ions increases, there is a corresponding increase in the particle size of the barium precursor M-hexaferrites. This observation is significant as it highlights that while the core structure remains stable, the dopant ions influence the morphology and potentially the magnetic properties of the material.

The coprecipitation method involves the simultaneous precipitation of barium, iron, cobalt, and zinc ions from an aqueous solution, followed by thermal treatment. This method is preferred for its simplicity and ability to produce uniform nanoparticles. During the synthesis process, the solution containing the metal ions is adjusted to an appropriate pH, causing the metals to precipitate as hydroxides. These hydroxides are then subjected to a calcination process, resulting in the formation of barium M-hexaferrite. The DTA/TGA analysis provides critical insights into the thermal stability and phase transitions of the synthesized material. The exothermic peaks observed in the DTA curves correspond to the phase transitions, including the formation of the hematite phase at higher temperatures. The TGA analysis indicates weight loss events, which are associated with the decomposition of intermediate phases and the release of volatile components. XRD analysis further confirms the phase purity and crystallinity of the synthesized barium M-hexaferrite. The diffraction patterns indicate that the hexagonal structure is preserved across different doping levels, supporting the notion that Co and Zn ions are successfully incorporated into the Fe sites without disrupting the overall lattice structure. Moreover, the particle size analysis underscores the impact of dopant concentration on the material's morphology. As the amount of Co/Zn dopant increases, the particle size of the synthesized hexaferrite also increases, which could be attributed to the changes in the nucleation and growth mechanisms during the synthesis process. This size variation is crucial as it can influence the magnetic properties of the material, which are essential for various applications in magnetic storage and electronic devices.

In conclusion, the coprecipitation method for synthesizing barium M-hexaferrite $BaFe_{12-2x}Co_xZn_xO_{19}$ is effective and produces high-purity nanoparticles with controllable size and phase composition. The introduction of Co/Zn dopants enhances the material properties without altering its fundamental structure, making this method suitable for advanced material engineering and application in various technological fields.

RECOMMENDATION

For future research, it is recommended to explore the optimization of the co-precipitation synthesis parameters further, such as dopant concentration, temperature, and pH, to enhance the phase purity and magnetic properties of barium M-hexaferrites. Additionally, investigating the impact of different dopants or combinations of dopants on the material's structural and magnetic properties could provide deeper insights and potentially lead to the development of novel materials with improved performance. Finally, extending the application testing of M-hexaferrites in real-world conditions would be beneficial to validate their practical utility and durability.

ACKNOWLEDGEMENT

We would like to express our gratitude to all those who contributed to this research through their guidance, technical assistance, and valuable insights. Special thanks to our colleagues and the technical staff for their support in this study.

REFERENCES

Abbasi, A., Ghanbari, D., Salavati-Niasari, M., & Hamadanian, M. (2016). Photo-degradation of methylene blue: Photocatalyst and magnetic investigation of Fe2O3–TiO2 nanoparticles and nanocomposites. *Journal of Materials Science: Materials in Electronics*, *27*(5), 4800–4809. https://doi.org/10.1007/s10854-016-4361-4

Ahmed, M. A., Okasha, N., & Kershi, R. M. (2008). Influence of rare-earth ions on the structure and magnetic properties of barium W-type hexaferrite. *Journal of Magnetism and Magnetic Materials*, *320*(6), 1146–1150. https://doi.org/10.1016/j.jmmm.2007.11.014

Ai, L.-H., & Jiang, J. (2009). Rapid synthesis of nanocrystalline Co3O4 by a microwave-assisted combustion method. *Powder Technology*, *195*(1), 11–14. https://doi.org/10.1016/j.powtec.2009.05.006

Almessiere, M. A., Slimani, Y., Sertkol, M., Nawaz, M., Baykal, A., & Ercan, I. (2019). The impact of Zr substituted Sr hexaferrite: Investigation on structure, optic and magnetic properties. *Results in Physics*, *13*, 102244. https://doi.org/10.1016/j.rinp.2019.102244

Anand, S., Pauline, S., & Prabagar, C. J. (2020). Zr doped Barium hexaferrite nanoplatelets and RGO fillers embedded Polyvinylidenefluoride composite films for electromagnetic interference shielding applications. *Polymer Testing*, *86*, 106504. https://doi.org/10.1016/j.polymertesting.2020.106504

Awadallah, A., Mahmood, S. H., Maswadeh, Y., Bsoul, I., Awawdeh, M., Mohaidat, Q. I., & Juwhari, H. (2016). Structural, magnetic, and Mössbauer spectroscopy of Cu substituted M-type hexaferrites. *Materials Research Bulletin*, *74*, 192–201. https://doi.org/10.1016/j.materresbull.2015.10.034

Bañuelos-Frías, A., Martínez-Guajardo, G., Alvarado-Perea, L., Canizalez-Dávalos, L., Ruiz, F., & Valero-Luna, C. (2019). Light absorption properties of mesoporous barium hexaferrite, BaFe12O19. *Materials Letters*, *252*, 239–243. https://doi.org/10.1016/j.matlet.2019.05.137

Bayrakdar, H., Yalçın, O., Vural, S., & Esmer, K. (2013). Effect of different doping on the structural, morphological and magnetic properties for Cu doped nanoscale spinel type ferrites. *Journal of Magnetism and Magnetic Materials*, *343*, 86–91. https://doi.org/10.1016/j.jmmm.2013.04.079

Cheng, Z., Zhang, J., & Kronmüller, H. (2003). Magnetically soft phase in magnetization reversal processes of nanocomposite Sm 2 Fe 15 Ga 2 C x / α − Fe permanent magnetic materials. *Physical Review B*, *68*(14), 144417. https://doi.org/10.1103/PhysRevB.68.144417

Feng, Y. B., Qiu, T., & Shen, C. Y. (2007). Absorbing properties and structural design of microwave absorbers based on carbonyl iron and barium ferrite. *Journal of Magnetism and Magnetic Materials*, *318*(1–2), 8–13. https://doi.org/10.1016/j.jmmm.2007.04.012

Gultom, G., Rianna, M., Sebayang, P., & Ginting, M. (2020). The effect of Mg–Al binary doped barium hexaferrite for enhanced microwave absorption performance. *Case Studies in Thermal Engineering*, *18*, 100580. https://doi.org/10.1016/j.csite.2019.100580

Hähsler, M., Zimmermann, M., Heißler, S., & Behrens, S. (2020). Sc-doped barium hexaferrite nanodiscs: Tuning morphology and magnetic properties. *Journal*

of Magnetism and Magnetic Materials, *500*, 166349. https://doi.org/10.1016/j.jmmm.2019.166349

Harris, V. G., Geiler, A., Chen, Y., Yoon, S. D., Wu, M., Yang, A., Chen, Z., He, P., Parimi, P. V., Zuo, X., Patton, C. E., Abe, M., Acher, O., & Vittoria, C. (2009). Recent advances in processing and applications of microwave ferrites. *Journal of Magnetism and Magnetic Materials*, *321*(14), 2035–2047. https://doi.org/10.1016/j.jmmm.2009.01.004

Kanagesan, S., Jesurani, S., Sivakumar, M., Thirupathi, C., & Kalaivani, T. (2011). Effect of Microwave Calcinations on Barium Hexaferrite Synthesized via Sol-Gel Combustion. *Journal of Scientific Research*, *3*(3), 451–456. https://doi.org/10.3329/jsr.v3i3.6483

Kaur, J., Sharma, V., Sharma, V., Veerakumar, V., & Kuanr, B. K. (2016). Fabrication and characterization of magnetically tunable metal-semiconductor schottky diode using barium hexaferrite thin film on gold. *AIP Advances*, *6*(5), 055820. https://doi.org/10.1063/1.4944522

Koutzarova, T., Kolev, S., Ghelev, Ch., Nedkov, I., Vertruen, B., Cloots, R., Henrist, C., & Zaleski, A. (2013). Differences in the structural and magnetic properties of nanosized barium hexaferrite powders prepared by single and double microemulsion techniques. *Journal of Alloys and Compounds*, *579*, 174–180. https://doi.org/10.1016/j.jallcom.2013.06.049

Lin, Y., Liu, Y., Dai, J., Wang, L., & Yang, H. (2018). Synthesis and microwave absorption properties of plate-like $BaFe_{12}O_{19}Fe_3O_4$ core-shell composite. *Journal of Alloys and Compounds*, *739*, 202–210. https://doi.org/10.1016/j.jallcom.2017.12.086

Pathak, N., Gupta, S. K., Sanyal, K., Kumar, M., Kadam, R. M., & Natarajan, V. (2014). Photoluminescence and EPR studies on Fe^{3+} doped $ZnAl_2O_4$: An evidence for local site swapping of Fe3+ and formation of inverse and normal phase. *Dalton Transactions*, *43*(24), 9313. https://doi.org/10.1039/c4dt00741g

Primc, D., Makovec, D., Lisjak, D., & Drofenik, M. (2009). Hydrothermal synthesis of ultrafine barium hexaferrite nanoparticles and the preparation of their stable suspensions. *Nanotechnology*, *20*(31), 315605. https://doi.org/10.1088/0957-4484/20/31/315605

Pullar, R. C. (2012). Hexagonal ferrites: A review of the synthesis, properties and applications of hexaferrite ceramics. *Progress in Materials Science*, *57*(7), 1191–1334. https://doi.org/10.1016/j.pmatsci.2012.04.001

Rösler, S., Wartewig, P., & Langbein, H. (2003). Synthesis and characterization of hexagonal ferrites $BaFe_{12-2x}Zn_xTi_xO_{19}$ ($0 \leq x \leq 2$) by thermal decomposition of freeze-dried precursors. *Crystal Research and Technology*, *38*(11), 927–934. https://doi.org/10.1002/crat.200310115

Rusianto, T., Waziz Wildan, M., Abraha, K., & Kusmono, K. (2015). Characterizations of Ceramic Magnets from Iron Sand. *International Journal of Technology*, *6*(6), 1017. https://doi.org/10.14716/ijtech.v6i6.1572

Shao, L.-H., Shen, S.-Y., Zheng, H., Zheng, P., Wu, Q., & Zheng, L. (2018). Effect of Powder Grain Size on Microstructure and Magnetic Properties of Hexagonal Barium Ferrite Ceramic. *Journal of Electronic Materials*, *47*(7), 4085–4089. https://doi.org/10.1007/s11664-018-6301-y

Suasmoro, S., Pratapa, S., Hartanto, D., Setyoko, D., & Dani, U. M. (2000). The characterization of mixed titanate Ba1−xSrxTiO3 phase formation from oxalate coprecipitated precursor. *Journal of the European Ceramic Society*, *20*(3), 309–314. https://doi.org/10.1016/S0955-2219(99)00143-0

Ting, T.-H., & Wu, K.-H. (2010). Synthesis, characterization of polyaniline/BaFe12O19 composites with microwave-absorbing properties. *Journal of Magnetism and Magnetic Materials*, *322*(15), 2160–2166. https://doi.org/10.1016/j.jmmm.2010.02.002

Wang, H., Xu, Y., Jing, L., Huang, S., Zhao, Y., He, M., Xu, H., & Li, H. (2017). Novel magnetic BaFe12O19/g-C3N4 composites with enhanced thermocatalytic and photo-Fenton activity under visible-light. *Journal of Alloys and Compounds*, *710*, 510–518. https://doi.org/10.1016/j.jallcom.2017.03.144

Wu, K. H., Ting, T. H., Wang, G. P., Yang, C. C., & Tsai, C. W. (2008). Synthesis and microwave electromagnetic characteristics of bamboo charcoal/polyaniline composites in 2–40GHz. *Synthetic Metals*, *158*(17–18), 688–694. https://doi.org/10.1016/j.synthmet.2008.04.013

Yu, H.-F., & Liu, P.-C. (2006). Effects of pH and calcination temperatures on the formation of citrate-derived hexagonal barium ferrite particles. *Journal of Alloys and Compounds*, *416*(1–2), 222–227. https://doi.org/10.1016/j.jallcom.2005.08.024

Zhang, W., Sun, A., Pan, X., Han, Y., Zhao, X., Yu, L., Zuo, Z., & Suo, N. (2020). Magnetic transformation of Zn-substituted Mg-Co ferrite nanoparticles: Hard magnetism → soft magnetism. *Journal of Magnetism and Magnetic Materials*, *506*, 166623. https://doi.org/10.1016/j.jmmm.2020.166623

Zhao, T., Jin, W., Wang, Y., Ji, X., Yan, H., Xiong, C., Lou, X., Dang, A., Li, H., & Li, T. (2017). In situ synthesis and electromagnetic wave absorbing properties of sandwich microstructured graphene/La-doped barium ferrite nanocomposite. *RSC Advances*, *7*(59), 37276–37285. https://doi.org/10.1039/C7RA06716J